NeuroImage 145 (2017) 377–388

Contents lists available at ScienceDirect

NeuroImage

journal homepage: www.elsevier.com/locate/ynimg

The Virtual Epileptic Patient: Individualized whole-brain models of epilepsy spread

V.K. Jirsa [a,*], T. Proix [a], D. Perdikis [a], M.M. Woodman [a], H. Wang [a], J. Gonzalez-Martinez [d], C. Bernard [a], C. Bénar [a], M. Guye [c], P. Chauvel [a,d], F. Bartolomei [a,b]

[a] Aix Marseille Univ, INSERM, INS, Inst Neurosci Syst, Marseille, France
[b] Epileptology Department, and Clinical Neurophysiology Department, Assistance Publique des Hôpitaux de Marseille, Marseille, France
[c] Aix Marseille Univ, CNRS, CRMBM, Marseille, France
[d] Epilepsy Center, Cleveland Clinic, Cleveland, OH, USA

ARTICLE INFO

Article history:
Received 19 October 2015
Accepted 20 April 2016
Available online 28 July 2016

ABSTRACT

Individual variability has clear effects upon the outcome of therapies and treatment approaches. The customization of healthcare options to the individual patient should accordingly improve treatment results. We propose a novel approach to brain interventions based on personalized brain network models derived from non-invasive structural data of individual patients. Along the example of a patient with bitemporal epilepsy, we show step by step how to develop a Virtual Epileptic Patient (VEP) brain model and integrate patient-specific information such as brain connectivity, epileptogenic zone and MRI lesions. Using high-performance computing, we systematically carry out parameter space explorations, fit and validate the brain model against the patient's empirical stereotactic EEG (SEEG) data and demonstrate how to develop novel personalized strategies towards therapy and intervention.

Introduction

Personalized medicine proposes the customization of healthcare with medical decisions, practices and products being tailored to the individual patient. Individual variability has clear effects upon the responsiveness to treatment approaches, thus diagnostic testing is often employed for selecting appropriate and optimal therapies based on the context of a patient's genetic content or other molecular and cellular analysis. Historically personalized medicine uses heavily genetic information, but finds more and more viability on the systems level. Structural and functional neuroimaging play a key role and have already contributed concrete diagnostic tools that are though mostly restricted to neurology, e.g., such as presurgical evaluation of epilepsy or differential diagnosis of coma. Other domains such as psychiatry suffer from a void of diagnostic tools for routine clinical practice.

One solution to this issue that has been proposed by several groups is to link the interpretation of neuroimaging signals to computational brain models (Deco et al., 2011; Friston et al., 2014; Jirsa et al., 2010; Stephan and Mathys, 2014; Stephan et al., 2015). (Jirsa et al., 2002) proposed the use of connectivity (later referred to as the connectome, Sporns et al., 2005) derived from Diffusion-weighted MRI (dMRI) to constrain large-scale brain network models. An upsurge of connectome-based model development followed with applications to the resting state (Deco et al., 2009; Ghosh et al., 2008; Honey et al., 2007), aging (Nakagawa et al., 2013), and pathologies such as schizophrenia (Deco and Kringelbach, 2014) and lesions (Falcon et al., 2015). So far, modeling has focused on reproducing the set of functionally active links between brain areas (the so-called functional connectivity), but has been hampered by the stationary nature of most connectivity-based metrics applied to validate the models (Hansen et al., 2014). In fact, most meaningful situations and tasks in neuroscience pose themselves as non-stationary processes including the resting state, as well as cognitive and motor behaviors (Allen et al., 2012; Hansen et al., 2014). The same applies to pathological behaviors also, of which seizure recruitment, the focus of the current article, is only one example.

Here we argue that large-scale brain network models may make the link between non-stationary network dynamics (such as seizure propagation) and person-specific structural indicators including connectivity. We take advantage of two recent developments in system neuroscience that is adding Connectomics to Genomics in personalized medicine, and using patient-specific connectomes in large-scale brain networks as generative models of neuroimaging signals. To successfully make this link, three requirements need to be satisfied:

1. Demonstration of systematic and reproducible variation of structural connectomes across subjects (Bernhardt et al., 2013; Besson et al.,

* Corresponding author.
E-mail address: viktor.jirsa@univ-amu.fr (V.K. Jirsa).

http://dx.doi.org/10.1016/j.neuroimage.2016.04.049

2014). An obvious prerequisite is that dMRI sufficiently faithfully reconstructs individual connectomes. Validation studies have demonstrated good reliability of dMRI when state-of-the-art acquisition and post-processing techniques are applied (Knösche et al., 2015; Seehaus et al., 2013).
2. Existence of a link between individual structural and functional variation. At the group level, patterns of whole-brain connectome alterations were proven to distinguish left from right temporal lobe epilepsy (Besson et al., 2014; Wirsich et al., 2016.). At the individual level, resting state studies in healthy and pathological brains have established the predictive value of structural connectivity (Falcon et al., 2015; Finn et al., 2015).
3. Demonstration of explanatory power of connectome-based large-scale brain models. (Deco et al., 2014) showed that the structure-function relation is maximal when the global network dynamics approaches criticality. Further support of this link is provided by the derivation of the well-known resting state network patterns from connectome-based models in spontaneous conditions (Hansen et al., 2014) and following stimulation (Spiegler et al., in press). This link justifies clustering of patients into subpopulations of clinical functional relevance.

There is thus evidence indicating that all three criteria may indeed be satisfied, at least for certain cases including epilepsy and lesions and careful choice of the validation metrics. Under these conditions a virtualization strategy needs to be established, which is the objective of this article, and systematically validated. We present our systematic virtualization approach of an individual patient's brain along the example of epilepsy spread and define the Virtual Epileptic Patient (VEP) model, thereby identifying the key challenges along its way. All steps can be performed within the neuroinformatics platform The Virtual Brain (see http://www.thevirtualbrain.org; (Sanz Leon et al., 2013, 2015 Spiegler and Jirsa, 2013)) and its associated pipelines (Schirner et al., 2015; Proix et al., 2016).

Our approach to build the VEP brain model comprises the following steps:

i) Structural network modeling: non-invasive structural neuroimaging using MRI and dMRI allows the reconstruction of the patient's individual brain network topography and connection topology within the 3D physical space.
ii) Functional network modeling: Neural population models are defined on each network node. For epilepsy, our preferred model is the Epileptor, which comprises variables for the fast discharges and the slow energetic processes. Couplings between Epileptors are defined using the patient's connectome, that is the complete set of reconstructed white matter tracts
iii) Hypothesis formulation: Structural anomalies such as hamartoma, pachygyria, etc. (as observed for instance in the MRI) are identified within the network. Non-invasive functional neuroimaging further informs the expert clinician on the evolution of the epileptic seizure and allows the formulation of first hypotheses of the location of the Epileptogenic Zone (EZ), here defined as the hypothetical area in the brain responsible for the origin and early organization of the epileptic activity (Talairach and Bancaud, 1966). The Propagation Zone (PZ) comprises areas that are recruited during the seizure evolution, but are by themselves not epileptogenic. Parameters (epileptogenicity, anomalies) are set in the network model following the hypothesis on EZ (Bartolomei et al., 2013).
iv) Evaluation of the VEP brain model: The patient's brain network model is evaluated via simulation, data fitting and mathematical analysis. It can be used to either "fingerprint" individual patient brains by identifying a personalized parameter set through data fitting or according to clinical criterion. Systematic computational simulations will further generate parameter maps outlining the zones of seizures and seizure freedom. These maps will give guidance of how to tune model parameters (patient charts). The result of this evaluation predicts the most likely propagation patterns through the patient's brain and allows the exploration of brain intervention strategies.

In the following we demonstrate all steps necessary to build a VEP model for a particular patient. We simulate and analyze the VEP model. In particular we show parametric analyses of the VEP model and fit it against functional stereotactic EEG (SEEG) data. Finally we discuss the limits of its interpretation and point out future avenues for VEP modeling.

Materials and methods

Patient data

The patient is a right-handed 41-year-old female initially diagnosed with bitemporal epilepsy. The patient underwent comprehensive presurgical evaluation, including clinical history, neurological examination, neuropsychological testing, structural and diffusion MRI scanning, EEG and stereotactic EEG (SEEG) recordings along with video monitoring. Nine SEEG electrodes were placed in critical regions (see Table 1) based on the presurgical evaluation. SEEG electrodes comprise 10 to 15 contacts. Each contact is 2 mm of length, 0.8 mm in diameter and is 1.5 mm apart from other contacts. Brain signals were recorded using a 128-channel Deltamed™ system (sampling rate: 512 Hz, hardware band-pass filtering: between 0.16 and 97 Hz).

Structural and diffusion MRI were acquired with a Siemens Magnetom Verio 3 T MR-Scanner Siemens, Erlangen, Germany). T1-weighted images were acquired with a MPRAGE-sequence (TR = 1900 ms, TE = 2.19 ms, voxel size $= 1 \times 1 \times 1$ mm^3, 208 slices). The diffusion acquisition used a DTI-MR sequence (angular gradient set of 64 directions, TR = 10.7 s, TE = 95 ms, 70 slices, voxel size $= 2 \times 2 \times 2$ mm^3, b-value = 1000 s/mm^2).

Structural reconstruction

The large-scale connectivity and the cortical surface of the patient were reconstructed using SCRIPTS (available on GitHub: https://github.com/timpx/scripts), a processing pipeline tailored for TVB (Proix et al., 2016). The pipeline uses FreeSurfer (Fischl, 2012), FSL (Jenkinson et al., 2012), remesher (Fuhrmann et al., 2010), and MRtrix (Smith et al., 2013, 2012; Tournier et al., 2007) to process T1 and dMRI scans. The brain is divided in several regions according to a parcellation template, which is used for whole brain tractography to develop the connectivity (number of streamlines) and delay (length of streamlines) matrices. Cortical and subcortical surfaces are reconstructed and downsampled, along with a mapping of vertices to corresponding region labels. All processed data are formatted to facilitate import into TVB.

Table 1
SEEG electrode locations for the virtualized patient. The prime in the electrode name indicates a left electrode. Often both internal and external structures are recorded with the internal and external contacts respectively.

Name of the electrode	External structure	Internal structure
B′ (left)	Anterior middle temporal gyrus	Hippocampus head
C′ (left)	Posterior middle temporal gyrus	Hippocampus tail
H′ (left)	Superior temporal gyrus	Thalamus
HH′ (left)	Frontal lobe	Hypothalamic hamartoma
OR′ (left)	Middle frontal gyrus	Orbitofrontal cortex
TB′ (left)	Inferior temporal gyrus	Entorhinal cortex
TP′ (left)	Temporal pole	Temporal pole
B (right)	Lateral temporal cortex (T2)	Hippocampus head
TP (right)	Temporal pole	Temporal pole

Network node and neural mass model

We use the Epileptor (Jirsa et al., 2014) as a network node model. The Epileptor comprises five state variables acting on three different time scales. On the fastest time scale, state variables x_1 and y_1 account for the fast discharges during the seizure. On the slowest time scale, the permittivity state variable z accounts for slow processes such as variation in extracellular ion concentrations (Heinemann et al., 1986), energy consumption (Zhao et al., 2011), and tissue oxygenation (Suh et al., 2006). The system exhibits fast oscillations during the ictal state through the variables x_1 and y_1. Autonomous switching between interictal and an ictal states is realized via the permittivity variable z through saddle-node and homoclinic bifurcation mechanisms for the seizure onset and offset, respectively. The switching is accompanied by a direct current (DC) shift, which has been recorded *in vitro* and *in vivo* (Ikeda et al., 1999; Jirsa et al., 2014; Vanhatalo et al., 2003). On the intermediate time scale, state variables x_2 and y_2 describe the spike-and-wave electrographic patterns observed during the seizure, as well as the interictal and preictal spikes when excited by the fastest system via the coupling $g(x_1)$. The Epileptor equations read as follows:

$$\dot{x}_1 = y_1 - f_1(x_1, x_2) - z + I_1$$
$$\dot{y}_1 = 1 - 5x_1^2 - y_1$$
$$\dot{z} = \frac{1}{\tau_0}(4(x_1 - x_0) - z)$$
$$\dot{x}_2 = -y_2 + x_2 - x_2^3 + I_2 + 0.002g(x_1) - 0.3(z - 3.5)$$
$$\dot{y}_2 = \frac{1}{\tau_2}(-y_2 + f_2(x_1, x_2))$$

where

$$f_1(x_1, x_2) = \begin{cases} x_1^3 - 3x_1^2 & \text{if } x_1 < 0 \\ \left(x_2 - 0.6(z-4)^2\right)x_1 & \text{if } x_1 \geq 0 \end{cases}$$

$$f_2(x_1, x_2) = \begin{cases} 0 & \text{if } x_2 < -0.25 \\ 6(x_2 + 0.25)x_1 & \text{if } x_2 \geq -0.25 \end{cases}$$

$$g(x_1) = \int_{t_0}^{t} e^{-\gamma(t-\tau)} x_1(\tau) \mathrm{d}t$$

and $x_0 = -1.6; \tau_0 = 2857; \tau_2 = 10; I_1 = 3.1; I_2 = 0.45; \gamma = 0.01$. The parameter x_0 controls the tissue excitability, and is epileptogenic triggering seizures autonomously, if x_0 is greater than a critical value, $x_{0C} = -2.05$; otherwise the tissue is healthy. I_1 and I_2 are passive currents setting the operating point of the Epileptor. The excitability parameter x_0 and its spatial distribution are the target of all parameter-fitting approaches described further on. The LFP is the directed sum of discharges, $-x_1 + x_2$. Detailed bifurcation analyses of these parameters have been performed by El Houssaini et al. (2015).

Definition of the network and the epileptogenic zone

We couple the network nodes by permittivity coupling (Proix et al., 2014), which quantifies the influence of neuronal fast discharges x_{1j} of a remote region j on the local slow permittivity variable of region i. Changes in ion homeostasis are influenced by both local and remote neuronal discharges via a linear difference coupling function, which quantifies the deviation from the interictal stable state as a perturbation perpendicular to the synchronization manifold. The linearity is justified as a first order approximation of the Taylor expansion around the synchronized solution (Proix et al., 2014). Then permittivity coupling further includes the connectome C_{ij}, a scaling factor G, which both are absorbed in $K_{ij} = GC_{ij}$. The permittivity coupling from area j to area i reads $\sum_{j=1}^{N} K_{ij} \cdot (x_{1,j}(t - \tau_{ij}) - x_{1,j}(t))$, where τ_{ij} denotes the signal transmission delay. Here we neglect the signal transmission time delays, because we do not consider synchronization effects, but rather only epileptic spread, which is determined by the slow dynamics of the permittivity coupling. Mathematically, then the full VEP brain model equations read as follows:

$$\dot{x}_{1,j} = y_{1,i} - f_1(x_{1,i}, x_{2,i}) - z_i + I_{1,i}$$
$$\dot{y}_{1,i} = 1 - 5(x_{1,i})^2 - y_{1,i}$$
$$\dot{z}_i = \frac{1}{\tau_0}\left(4(x_1 - x_0) - z_i - \sum_{j=1}^{N} K_{ij} \cdot (x_{1,j} - x_{1,i})\right)$$
$$\dot{x}_{2,i} = -y_{2,i} + x_{2,i} - (x_{2,i})^3 + I_{2,i} + 0.002g(x_{1,i}) - 0.3(z_i - 3.5)$$
$$\dot{y}_{2,i} = \frac{1}{\tau_2}(-y_{2,i} + f_2(x_{1,i}, x_{2,i}))$$

To define the EZ, we defined a spatial map of epileptogenicity where each node was characterized by an excitability value x_0, which quantifies the ability of an Epileptor to trigger a seizure. For an isolated Epileptor, $G = 0$, the Epileptor can trigger seizures autonomously if $x_0 > x_{0c}$ and is referred to as epileptogenic; inversely if $x_0 < x_{0c}$, the Epileptor does not trigger seizures autonomously and is not epileptogenic. The spatial map of epileptogenicity comprises the excitability values of the EZ, the PZ and all other regions (see Fig. 1). Note that only nodes in the EZ discharge autonomously while embedded in the network (for $G \neq 0$). For the simulations, the different regions were set in the EZ or the PZ according to the clinician expertise (see Table 2).

Forward solutions

The functional data available for this patient includes SEEG, fMRI and EEG; however, in the following, we focus on the SEEG data as it plays the largest role in the clinical analysis. Like other modalities, the SEEG measurements can be modeled using a forward solution that describes the contribution of each source dipole to each contact's measurement. As with M/EEG, the patient's anatomy, specifically the so-called boundary elements of the brain-skull, skull-scalp and scalp-air interfaces may be taken into account, however unlike in M/EEG, boundary effects are usually insignificant and can be ignored for all contacts but those very close to the boundaries (Gramfort et al., 2010). We compute the potential for a point dipole in a homogeneous medium following (Sarvas,

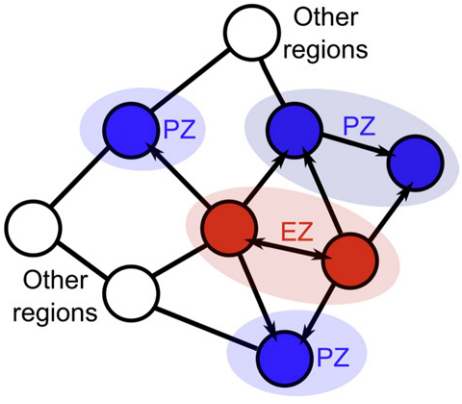

Fig. 1. Spatial distribution map of epileptogenicity. Isolated nodes outside of the network are epileptogenic for the critical value $x_{0C} = -2.05$. When embedded into the network, the nodes in the EZ (red) have a high excitability value ($x_0 > x_{0C} + 0.4$), whereas the nodes in the PZ (blue) have elevated excitability ($x_{0C} + 0.4 > x_0 > x_{0C}$). Finally, all other nodes (white) are not epileptogenic ($x_0 < x_{0C}$). EZ: left hippocampus, right hippocampus, left hypothalamus, right hypothalamus. PZ: left parahippocampal, left temporal pole, left parahippocampal, brainstem, left thalamus proper.

Table 2
Excitability values $x_0 = x_{0C} + \Delta x_0$ are expressed via their deviations Δx_0 from the critical value $x_{0C} = -2.05$. Positive Δx_0 indicates increased excitability. These excitability values are used to simulate the time series shown in Fig. 5.

Name of the region	Δx_0	Zones
Right hippocampus	1.3	EZ
Left hippocampus	0.4	EZ
Left hypothalamus	0.4	EZ
Right hypothalamus	0.4	EZ
Brain stem	0.31	PZ
Left parahippocampal	0.27	PZ
Left thalamus	0.24	PZ
Left temporal pole	0.16	PZ
Other regions	−0.2	Other regions

1987), ignoring the effect of source orientation, given that it is largely unknown for a given epileptic source and cannot be captured reliably at the resolution of a region-level brain network model. Dropping this factor from the lead field has, approximately, a spatial smoothing effect in cases where multiple areas contribute similarly to a given electrode, however given the sparsity of the lead field, the vast majority of electrodes effectively measures activity of a single area.

Anomalies in the MRI

Structural anomalies will require their integration into the model. Here we included a hypothalamic hamartoma in our virtualization via a modification of the local connectivity $K_{ij} = G_{hyp} C_{ij}$ of the hypothalamus. We delineated the hamartoma in the MRI scan and tractography and used the hypothalamic hamartoma as a seed region of interest to reconstruct its local connectivity. The local connectivity strength is scaled up parametrically by a scalar factor G_{hyp} to quantify the effect of the hamartoma without changing its local connection topology.

Data fitting

The target for all data fitting is the excitability parameter x_0, which may be set either to clinical criterion (see the Virtual Brain based simulations, EZ and PZ section) or estimated using more automated approaches. Obtaining such estimates of the parameters of the network model, given the available functional data is performed within a Bayesian framework, using a reduced Epileptor model (Proix et al., 2014) and reduced functional data set for the fitting. The SEEG data are windowed and Fourier transformed to obtain estimates of their spectral density over time (Bricolo et al., 1978). Then SEEG power above 10 Hz is summed to capture the temporal variation of the fast activity. These time series are corrected to a preictal baseline, log-transformed and linearly detrended over the time window encompassing the seizure (Makeig, 1993). Contacts are selected, which present greater high-frequency activity than their neighbors on the same electrode. Given that, contrary to M/EEG, the SEEG lead field is very sparse, three nodes per contact are used in the network model. Other nodes are not recruited and rest at their fixed points. We approximate this effect, in the fitting only, through a constant sum over the corresponding elements of the structural connectivity matrix. These elements correspond to areas, which neither participate in the seizure, nor have nearby depth electrodes and are thus observable only through network effects, whose hidden states prove uninformative and unreliable in their estimation. Next, we use an observation model that incorporates the SEEG forward solution described above, under the assumption that the x_1 variable describes fluctuations in the log power of high frequency activity, predicting sensor log power, with normally distributed observation error.

Hidden states in Bayesian modeling represent states of the generative model (variables, parameters) that are not directly observable. Uninformative priors are placed on the hidden states' initial conditions, while their evolution follows a Euler-Maruyama discretization of the corresponding stochastic differential equations with linear additive normally distributed noise. Uninformative priors are also placed on the excitability parameter per node x_0 observation baseline power, scale and noise. Finally the length of the seizure is also allowed to freely vary to match that of a given recorded seizure. Structural connectivity specifies a gamma prior on the connectivity used in the generative method. This model is implemented using Stan, a software for Bayesian inference, which implements both Hamiltonian Monte-Carlo and automatic variational inference algorithms for generic differential probability models (Hoffman and Gelman, 2011; The Stan Development Team, 2015). This approach takes advantage of the efficiency of the variational algorithm, which constructs an approximate proxy distribution on the true posterior optimized via stochastic gradient ascent (Kucukelbir et al., 2015).

Numerical methods

To simulate the system of stochastic differential equations, we used an Euler-Maruyama integration scheme with an integration step of 0.05. Additive white Gaussian noise was introduced in the variables x_2 and y_2 with mean 0 and variance 0.0025 (Jirsa et al., 2014). Other variables experienced only little or no noise due to their high sensitivity. 256 time steps are equivalent to one second of real time to obtain realistic frequency ranges, seizure lengths, and matched intracranial EEG sampling frequency. Whenever specified in the Results section, we used a bandpass Butterworth filter of order 5, with cut-off frequencies of 0.16 Hz and 97 Hz at −3 dB (Fig. 2D). The filter is identical to the one used to process intracranial EEG signals (see (Bartolomei et al., 2008) for processing methods of intracranial EEG signals). Finally, for the stimulated seizure, a rectangular function in time was applied on the z variable of the stimulated region (amplitude: 0.5, length: 2 s).

Results

Empirical patient data

The patient was diagnosed with bitemporal epilepsy and experienced simple and secondary generalized seizures, which were accompanied by déjà-vu hallucinations, associated with palpitations, horripilation, and frisson sensations. Fixed gaze, chewing up and pallor were observed during the seizure. In the post-critic period the patient showed temporal disorientation, repetition of the same questions and retrograde amnesia during one week. The MRI examination revealed a hypothalamic hamartoma. Surface EEG recordings revealed interictal spikes and indicated a bias towards the left hemisphere. Based on the presurgical evaluation, seven SEEG electrodes were implanted in the left hemisphere, and two in the right hemisphere. One electrode was implanted in the hypothalamic hamartoma. Fig. 2 shows the implantation sheme in the left column, color-coding the SEEG electrodes. During two weeks of continuous SEEG recordings, we recorded 6 simple seizures localized in the right hippocampus, and two complex seizures starting in the right hippocampus and then recruiting the left hippocampus, the left temporal lobe and the hypothalamic hamartoma. Representative seizure propagation patterns are shown in Fig. 2.

Connectivity patterns

We reconstructed the large-scale connectivity of the patient, in particular the weight and tract length matrices, using the pipeline described in the Structural reconstruction section. The tract length matrix divided by the signal transmission speed defines the time delays. The two matrices (see Fig. 3A and B) establish the space-time structure of the coupling (Jirsa, 2009) and allow a full virtualization of the patient's brain model. Fig. 3C shows the location of the hypothalamic hamartoma and 3D the reconstructed streamlines from the hypothalamus, which

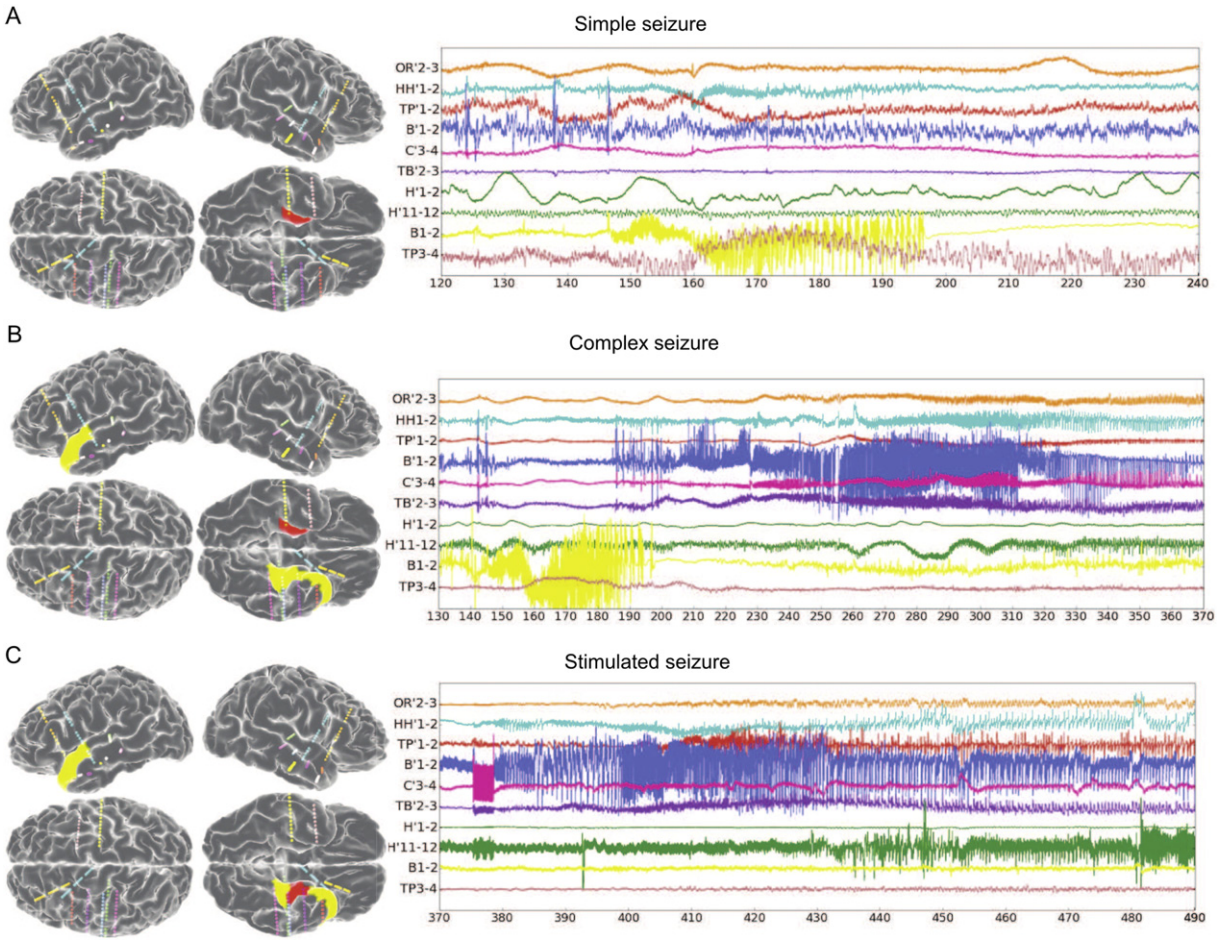

Fig. 2. Different types of epileptic seizures are recorded with SEEG electrodes in this patient. (A) Simple seizure. The simple seizures started in the right hippocampus (red zone on the left picture, channel B1–2 on the SEEG time series) and remained restricted to this area. (B) Complex seizure. The complex seizures started in the right hippocampus (channel B1–2) before spreading to the contralateral hippocampus (channel B′1–2) and further spreading in the left temporal lobe. (C) Stimulated seizure. After stimulating the left hippocampus (channel C′3–4), a seizure was triggered, spreading to the remainder of the left temporal lobe, but not propagating to the right hemisphere. In particular, the hypothalamic hamartoma was recruited.

we used to mimic the hypothalamic hamartoma and differentially weigh its influence on the network dynamics.

Virtual Brain based simulations, EZ and PZ

Each node of the network was occupied with an Epileptor, a neural mass model able to reproduce epileptic seizures dynamics (Jirsa et al., 2014). For the Epileptor in isolation (i.e. no network coupling), if $x_0 > x_{0C}$, the neural mass is above threshold: the Epileptor can trigger seizures and is said epileptogenic, and inversely if, $x_0 < x_{0C}$, the Epileptor does not trigger seizure and is said not epileptogenic. When embedded into a network, each network node's capacity of triggering seizures will then depend on its excitability and connectivity. The nodes were connected via permittivity coupling, which acts on a slow time scale and allow the spread of the seizure through the network by recruiting regions not in the EZ. In this section we set the excitability parameters for EZ, PZ and all other regions according to clinical criteria comprising (i) regions involved in the seizure; (ii) seizure length; (iii) length of time delays before recruitment of other regions; (iv) seizure frequency in each region. These criteria are used clinically in standard-of-care to evaluate the epileptogenicity of brain regions (Bartolomei et al., 2008, Proix et al., 2014). The spatial distribution of excitability was heterogeneous across the network (see Fig. 1), with high value of excitability for regions in the EZ ($x_0 \geq x_{0C} + 0.4$), smaller excitability values for regions in the PZ ($x_{0C} + 0.4 > x_0 \geq x_{0C}$), and other nodes not epileptogenic ($x_0 < x_{0C}$).

Once EZ and PZ were defined, a systematic parameter space exploration was performed by varying the following parameters: (i) the global coupling strength G, which is a scalar factor multiplying the whole connectivity matrix, (ii) the local coupling strength G_{hyp} of the hypothalamus, which is a scalar factor multiplying the contribution of the hypothalamus to the connectivity matrix, (iii) the excitability values $x_0^{\text{right hippocampus}}$ of the right hippocampus, (iv) the excitability values $x_0^{\text{Other regions}}$ of the regions not recruited in the propagation zone. The excitability values of the other regions in the EZ and the PZ were fixed (see Table 2). To describe the network behavior in the thus four-dimensional parameter space, we use the clinical criteria i) through iv) for seizure quantification. - Fig. 4 shows one of these quantifiers, the frequency of recruitment for three different regions in a seizure over a fixed simulation time as a function of the four parameters G, G_{hyp}, $x_0^{\text{right hippocampus}}$, and $x_0^{\text{Other regions}}$.

Fig. 4 illustrates an important deliverable of the VEP brain model, that is the results of the systematic parameter space explorations. These navigation charts offer the clinician a tool for decision-making and hypothesis building. For instance, Fig. 4 demonstrates for this particular patient that changes of excitability in the EZ regions show fairly little influence on the number of seizures in the VEP brain model, whereas reduction of excitability outside of EZ/PZ regions is linked to seizure reduction in the left thalamus and hypothalamus, and to a lesser extent in the left parahippocampus (Fig. 4A and B). A decrease of left hypothalamic connectivity will always cause an increase of seizures in the left hypothalamus, but not the left thalamus. The only means of

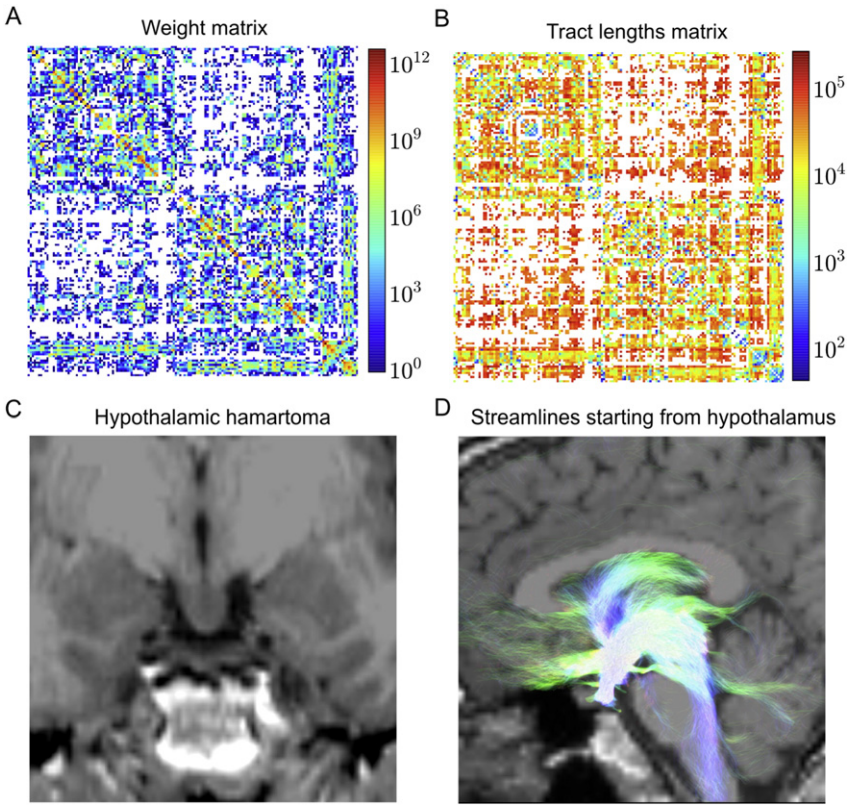

Fig. 3. (A) Structural connectivity matrix. (B) Tract lengths matrix. (C) MRI image showing the hypothalamic hamartoma. (D) Streamlines obtained by seeding from the hypothalamus. The direction of the streamline is indicated using a color code (red: left-right, blue: superior-inferior, green: anterior-posterior).

increasing the likelihood for seizures in the left thalamus is the increase of the scaling of global coupling G, while maintaining high values of hypothalamic connectivity (Fig. 4A). For all of the above scenarios, the left parahippocampus shows fairly high seizure numbers with one exception, that is high hypothalamic connectivity and low overall strength of global coupling G (Fig. 4C). These discussions demonstrate that the various parameter manipulations have inverse and non-trivial effects upon the seizure numbers in different brain regions. Changes in parameters are directly linked to therapeutic network interventions, though the link is not always evident, since the variation of a network parameter may find different realizations in clinical practice. For instance, the excitability of a brain region in the network node model is a key parameter, which is physiologically linked to variables such as balance of excitation and inhibition, local synaptic efficacy, extracellular ionic concentrations, or glial activity. Alterations of these variables will result in excitability changes in the tissue, and thus in the desired network effects predicted by the VEP brain model; however, they may also influence other network parameters within the model. This non-bijective mapping between model and physiological parameters thus poses a clinical challenge in terms of identification, but also allows the exploration of multiple therapeutic avenues to manipulate a model parameter and exploit the prognostic predictions of the VEP.

We selected a representative set of parameters ($G = 10$, $G_{hyp} = 10$, $\Delta x_0^{\text{right hippocampus}} = 1.3$, $\Delta x_0^{\text{Other regions}} = -0.2$; see red dot in Fig. 4) matching the patient's seizure with regard to the clinical criteria i) through iv). We simulated the brain network model over a period of 20 seizures and computed the forward solution for the SEEG electrodes (see Numerical methods). Simple seizures (Fig. 5A) and complex seizures (Fig. 5B) were generated with similar regions recruited compared to the real SEEG recordings (see Fig. 1A and B). We also stimulated the left hippocampus (Fig. 5C), and observed a propagation pattern in the left temporal lobe, similar to the SEEG recordings (Fig. 2C).

Fig. 6A shows the spatial extent of the EZ and the PZ such as estimated by clinician expertise. Fig. 6B shows the spatial extent of the excitability zone expressed through the parameter distribution of $x_0 = x_{0C} + \Delta x_0$, here illustrated via its deviations Δx_0 from the critical value $x_{0C} = -2.05$. These parameter settings are used for the simulation of Fig. 5 plotted over an MRI view. Fig. 6C shows the comparison of the distribution of excitabilities found by fitting the model to the SEEG data (as developed in the Data fitting section). Data fitting identifies a bilateral mesial temporal EZ, a result well in agreement with the clinical interpretation.

Data fitting

Inversion of the brain network model described above, with the primary goal of obtaining the spatial distribution of x_0 values, provides a set of samples from the posterior distribution of the model parameters given the data. The following results were obtained with the hamartoma included in the analysis. Fig. 7 shows the results of inversion on a section of SEEG containing a complex seizure. Fig. 7A shows in solid black lines the time course of the high-frequency power for two contacts which illustrate the start and interhemispheric propagation of the seizure. In

Fig. 4. Parameter space exploration for (a) left thalamus, (b) left hypothalamus, (c) left fusiform cortex. Excitability values $x_0 = x_{0C} + \Delta x_0$ are expressed via their deviations from the critical value $x_{0C} = -2.05$. Positive Δx_0 indicates increased excitability. The color indicates the number of recruitments of the region in the seizure over a simulation of fixed length in dependence of (i) global coupling strength g (y axis), (ii) local coupling strength for the hypothalamic connections G_{hyp} (x axis), (iii) the excitability $\Delta x_0^{\text{right hippocampus}}$ of the right hippocampus (each row is a different value), (iv) the excitability $\Delta x_0^{\text{Other regions}}$ of the regions not recruited in the propagation zone (each column is a different value). The red point indicates the parameter chosen for the simulation.

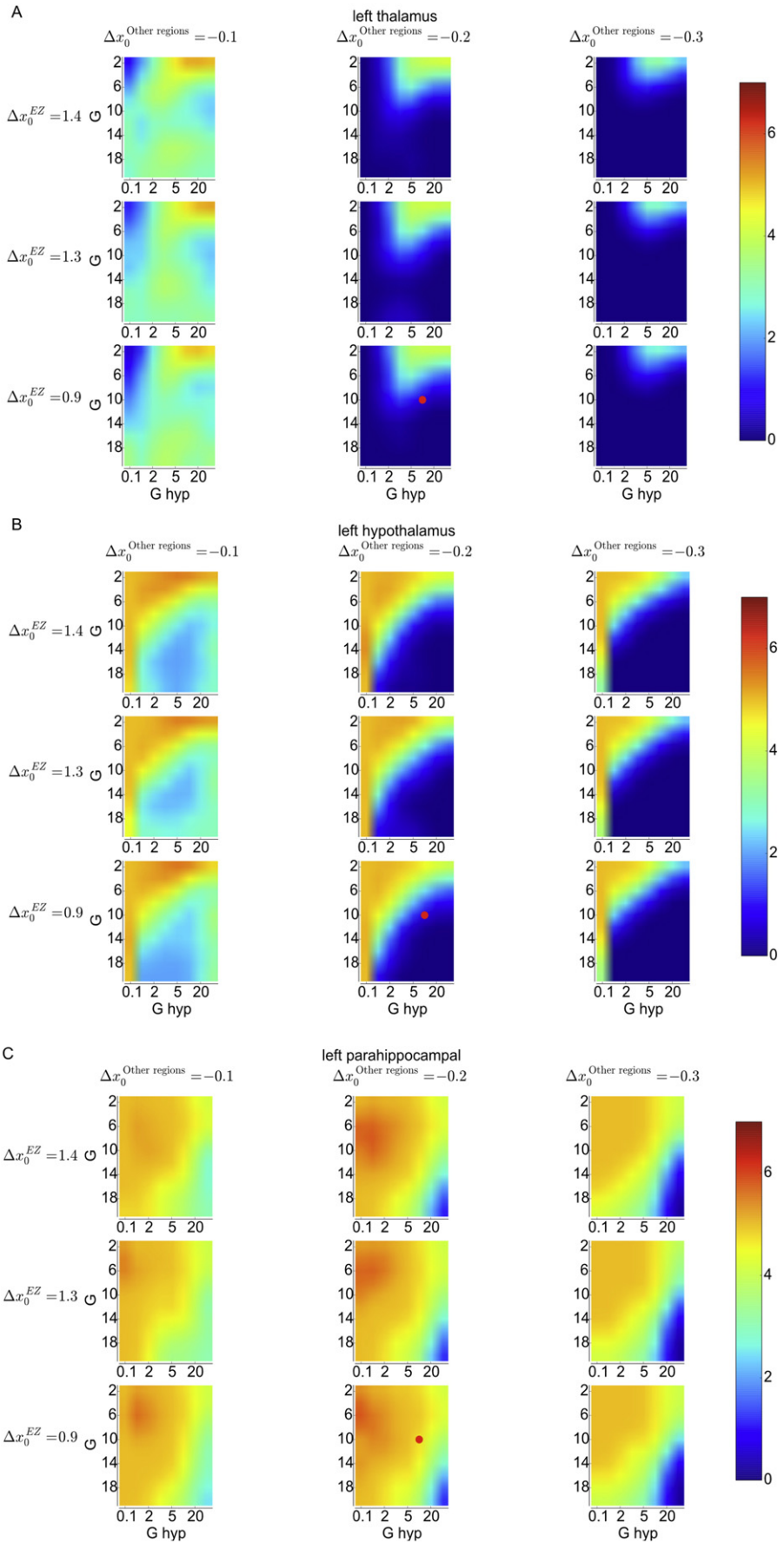
A
left thalamus
$\Delta x_0^{\text{Other regions}} = -0.1$
$\Delta x_0^{\text{Other regions}} = -0.2$
$\Delta x_0^{\text{Other regions}} = -0.3$
$\Delta x_0^{EZ} = 1.4$
$\Delta x_0^{EZ} = 1.3$
$\Delta x_0^{EZ} = 0.9$
G
2 6 10 14 18
0.1 2 5 20
G hyp
6 4 2 0
B
left hypothalamus
$\Delta x_0^{\text{Other regions}} = -0.1$
$\Delta x_0^{\text{Other regions}} = -0.2$
$\Delta x_0^{\text{Other regions}} = -0.3$
$\Delta x_0^{EZ} = 1.4$
$\Delta x_0^{EZ} = 1.3$
$\Delta x_0^{EZ} = 0.9$
G
2 6 10 14 18
0.1 2 5 20
G hyp
6 4 2 0
C
left parahippocampal
$\Delta x_0^{\text{Other regions}} = -0.1$
$\Delta x_0^{\text{Other regions}} = -0.2$
$\Delta x_0^{\text{Other regions}} = -0.3$
$\Delta x_0^{EZ} = 1.4$
$\Delta x_0^{EZ} = 1.3$
$\Delta x_0^{EZ} = 0.9$
G
2 6 10 14 18
0.1 2 5 20
G hyp
6 4 2 0

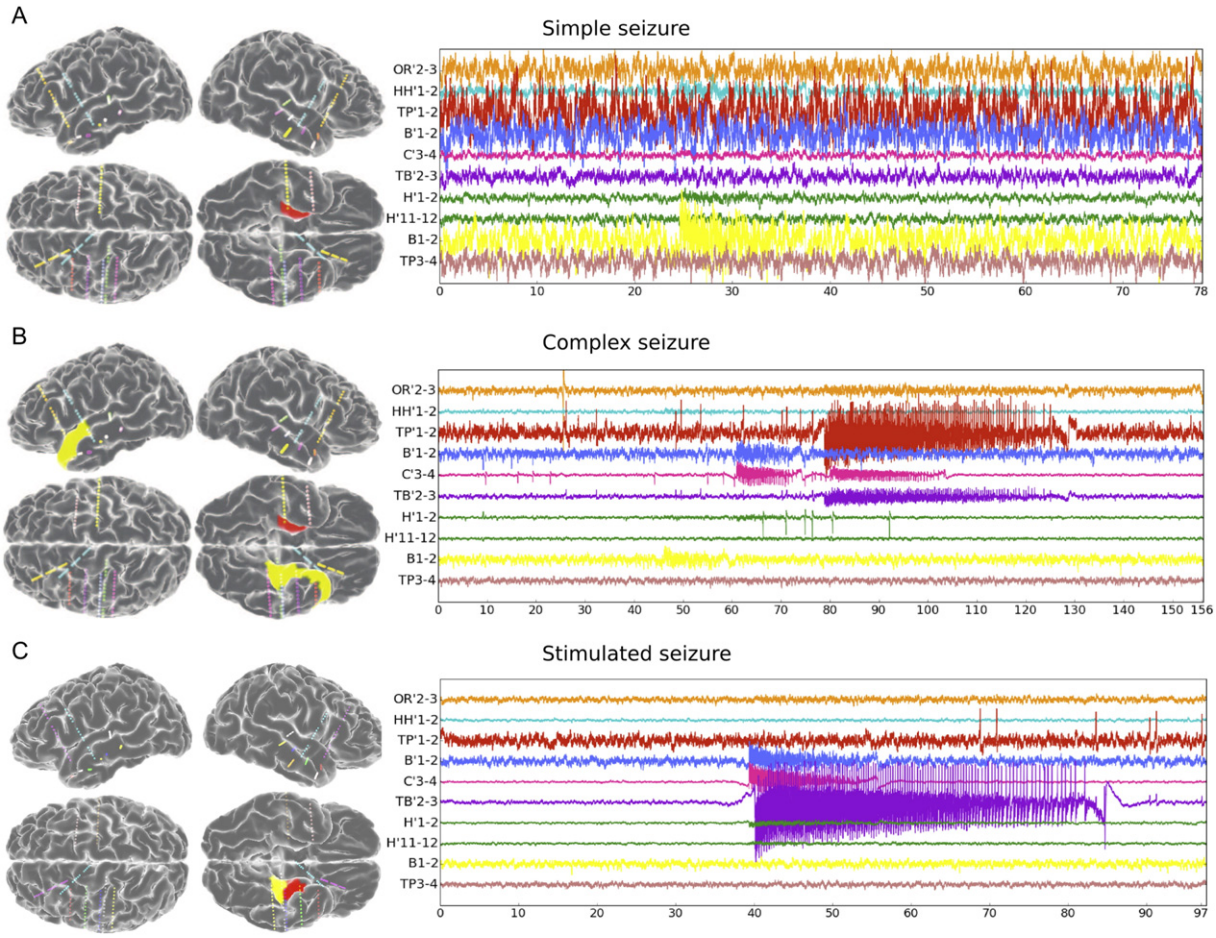

Fig. 5. Simulation of the different types of epileptic seizures for this patient. (A) Simple seizure. The simple seizure started in the right hippocampus (red zone on the left picture, channel B1–2 on the SEEG time series) and remained restricted to this area. (B) Complex seizure. The complex seizures started in the right hippocampus (channel B1–2) before spreading to the contralateral hippocampus (channel B′1–2) and further spreading in the left temporal lobe. (C) Stimulated seizure. After stimulating the left hippocampus (channel C′3–4), a seizure was triggered, recruiting the left temporal lobe.

order to assess the hidden state estimation, the hidden states are used to generate corresponding predictions for the SEEG power via the observation model described in the methods. The blue shading covers the 5th to 95th percentiles of the estimates. While the full Epileptor model can reproduce also the high-frequency states (spike-wave, fast oscillations), our choice of observation function makes the inference more tractable, at the loss of lumping these two states together under the observation function.

Fig. 7B shows the estimates of excitability for each network node included in the analysis. Region names are abbreviated as follows: CLE, left entorhinal cortex; CLLO, left lateral orbitofrontal; CLMT, left middle temporal; CLST, left superior temporal; CLTP, left temporal pole; CLTT, left transverse temporal; LP, left pallidum; LH left hippocampus; LA, left amygdala; RH, right hippocampus; RA, right amygdala; LHyp, left hypothalamus; RHyp, right hypothalamus. Posterior densities for the excitability parameter x_0 are illustrated by so-called violin plots, where the probability is proportional to the thickness of the yellow band. Extrema are shown by red ticks. The node corresponding to the right amygdala (RA) corresponds to the B2 SEEG electrode where this seizure starts, shows a high estimate for excitability. The left entorhinal

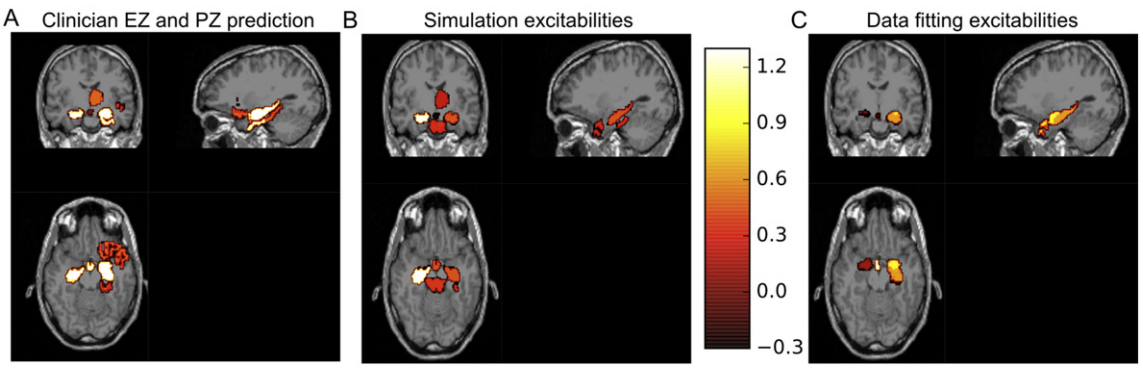

Fig. 6. Clinical interpretation of the distribution of excitability. (A) Clinician's prediction of EZ (in yellow) and PZ (in red) (B) and (C) show two distributions of excitability as used in the simulations: (B) shows the parameter set identified in Fig. 6, (C) show the distribution of excitability as found by the data fitting. The color bar is common for (B) and (C).

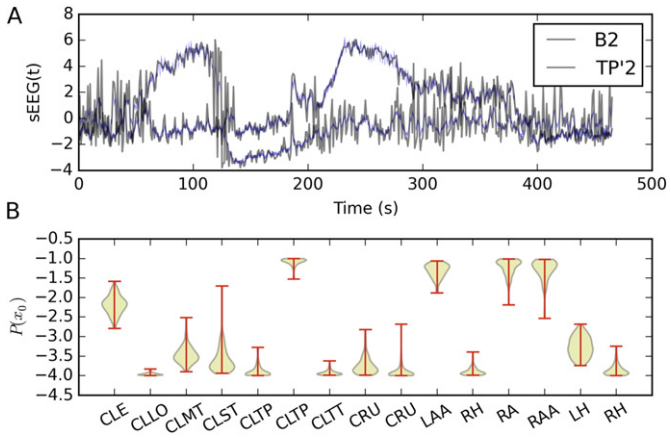

Fig. 7. Inversion of network model on complex seizure: (A) shows the true time course in solid black of high-frequency power of two SEEG channels, B2 where the seizure starts and TP'2 where the seizure propagates. Shown in blue is the predicted SEEG power based estimates of hidden states to which the observation model is applied, shaded to cover 5th to 95th percentiles. (B) Violin plots of the estimated densities of the x_0 parameter for nodes included in the analysis. Region RA or "Right Amygdala" corresponds to SEEG electrode B2, where the seizure starts, region CLE or left entorhinal cortex corresponds to SEEG electrode TP'2, where the seizure propagates. Region names' abbreviations are provided in the text.

cortex (CLE in Fig. 7B) corresponds to SEEG electrode TP'2, where the seizure can be seen to propagate in Fig. 7A. This node's x_0 estimate is ambiguous, as the threshold for epileptogenicity in the model is $x_0 = -2.1$. As inference generates not only point estimates, i.e. single values for parameters, but a distribution of the parameter values as shown in the violin plots, it is expected that the data confirm certain hypotheses and not others. Likewise, inference can generate informative estimates with small variance or uninformative estimates with high variance, depending on data. It is generally considered an advantage of Bayesian methodology that data, which do not inform about a parameter, provide uninformative results. The important conclusions are that the propagation of the seizure between areas is correctly reconstructed and that informative estimates can be obtained for the EZ (here, the right amygdala estimate is informative). Nevertheless, the estimates are generally informative, discriminating nodes as epileptogenic or not, but in some cases run into the upper or lower bounds placed on the uninformative prior on x_0 in $(-4$ to $-1)$.

Discussion

Despite the heavy sequelae from medically refractory epilepsy, there is a potentially curative procedure - surgical resection of the EZ (Najm et al., 2006; Rosenow and Lüders, 2001). However, to be effective, this procedure depends on correct identification of the EZ, which is often unclear (Bulacio et al., 2012). A comprehensive pre-surgical evaluation is necessary to pinpoint the EZ as well as to identify the risks of neurologic morbidity such as visual or speech impairment (Wyllie et al., 1988; Jayakar et al., 1994; Adelson et al., 1995; Jayakar, 1999). Various non-invasive and invasive methods are used. Non-invasive techniques include scalp EEG and video-EEG monitoring, neuropsychological tests, speech-language studies, and brain imaging (MRI, PET, Ictal SPECT). Of these methods, to this date the highest predictor of surgical success is identification of a single visible MRI lesion (Bulacio et al., 2012; Jeha et al., 2007; Lopez-Gonzalez et al., 2012). In patients with non-lesional MRI, localization and surgical success in seizure control are even more challenging (Jeha et al., 2007) Despite the advances in imaging technologies, a significant number of surgical patients with focal epilepsy (~25%) continues to have non-lesional MRIs (Jeha et al., 2007; Widdess-Walsh et al., 2007), which is a problem calling for novel approaches.

We propose such a novel approach to brain interventions based on large-scale brain network based models that are derived from non-invasive structural data of individual patients. Here we have shown step by step, along the example of a patient with bitemporal epilepsy, how to create a virtual patient brain network model. The Virtual Epileptic Patient (VEP) model provides the perfect test bed for clinical hypothesis testing of questions linked to network-based mechanisms. Questions outside of this framework will be more difficult or impossible to address by our macroscopic approach and are the focus of other efforts (Markram et al., 2015) emphasizing the microscopic approach. The latter approaches are a promising avenue for the future and will shed light on the physiological mechanisms and signaling pathways involved in pathologies; our macroscopic approach is feasible today and relates directly to the signals measured by modern brain imaging technologies.

Large-scale brain network models in general, and the VEP brain model in particular, have three critical components, network connectivity, neural mass model and MRI lesions. First, procedures to reconstruct connectivity from dMRI data nowadays reliably extract structural network connectivity with high anatomical precision (Johansen-Berg and Berhens, 2009) and efforts are on the way to develop more advanced methods proving robust and reproducible on subject and group levels (Besson et al., 2014). Thus there is hope that patient specific connectomes may soon enter in clinical routine use. Second, neural mass models are placed at the network nodes and determine the dynamic nature of the interactions. Neural mass models need not necessarily to be derived from biophysical mechanisms, but rather need to capture the dynamic repertoire of the neural population. It is in this dynamical sense that they have to be biophysically realistic, not in the traditional bottom-up causal sense. In epilepsy, the Epileptor is a neural mass model that has been derived purely based on mathematical reasoning. It provides a complete taxonomy of epileptic seizures including onset, offset and seizure evolution characteristics. Once a seizure type has been determined for a particular patient, then the taxonomy by (Jirsa et al., 2014) offers a mathematical formulation of a generative model that can be used as a network node in the VEP model. Third, integration of MRI lesions into the VEP model is possible, but not evident due to the challenge in translating the lesion into model parameters. Reasonable candidates are excitability and local connectivity, because localized tissue abnormalities are likely to alter these two parameters in the context of our network perspective. MRI lesions provide a spatial map of altered parameters that thus enter into the VEP model and affect the network dynamics. The emergent dynamic effects, that are the seizures in the current context, will crucially depend on the interplay between network node model (Epileptor), patient specific structural connectivity (from dMRI), and spatial maps of excitability (EZ, PZ) and MRI lesions.

Translating the VEP model to the patient bed will require then quantification of the model outcomes through parameter space analyses and data fitting. In combination, these two will allow systematic discovery and development of novel therapies and interventions. For the specific case of our patient, we find excellent correspondence of the spatiotemporal seizure evolution between simulation and empirical data. (Proix et al., under review, 2016) demonstrate a good correlation ($N = 15$ patients) between (non-invasive) VEP-based prediction of EZ/PZ and the clinical expert's opinion based on (invasive) SEEG analysis. Their analysis shows that the use of individual connectomes derived from a patient's DTI improves the prediction significantly. These results are consistent with structural differences between dMRI measures across patients, showing reduced fractional anisotropy (Ahmadi et al. 2009; Bernhardt et al., 2013) and structural alterations in the connectome of epileptic patients (Bonilha et al., 2012; DeSalvo et al., 2014, Besson et al., 2014; Wirsich et al., 2016). Dramatic structural changes may be induced by lesions or tumors changing the topology of the structural network and thus may alter the dynamical properties of seizure recruitment. We demonstrated this in Fig. 4, where the inclusion of the hypothalamic lesion modifies the spatial recruitment pattern. For the present

patient and one fixed parameter set, the VEP model captures both, simple and complex seizure spread (Fig. 5A and B), as well as the responses towards stimulation (Fig. 5C). The spatiotemporal organization of EZ and PZ matches both empirical data (Figs. 2 and 6A) and simulations (Fig. 5). The distribution of excitability values (Fig. 6B and C) is not trivially linked to the recruitment of PZ. This becomes evident when the associated parameter spaces are considered (Fig. 4). As local connectivity of the hypothalamus increases, the number of seizures reduces generally in the left thalamus, left hypothalamus and left parahippocampus, if the overall coupling strength G is sufficiently large. This stabilization appears to be predominantly a network effect due to the stabilization through the residual network. As the thalamus is well connected to the hypothalamus, an increase of G_{hyp} destabilizes the thalamic equilibrium, but reciprocally stabilizes the hypothalamus. This reasoning applies to all regions directly connected to the hypothalamus, identifying a prominent local network in this patient's seizure dynamics. Increasing the excitability in the residual network (other regions, Fig. 4A) alters the parameter space of the thalamus such that seizure propensity is indeed minimal for small global connectivity G, but forces the parahippocampus and hypothalamus into a high-seizure regime, thus does not provide a viable option for seizure reduction of the entire brain network. Hence the best strategy to avoid complex seizures and seizure propagation in this patient remains the navigation into the region of the parameter space with increased global coupling G and local hypothalamic coupling G_{hyp}. This therapeutic option is valid for the patient's present connectome, which leaves these parameter spaces intact. Alternatively, surgical interventions are a means of manipulating the connectome and, subsequently, reshaping the parameter spaces with the target of increasing the (blue) regions of low seizure propensity in Fig. 4.

To improve surgical outcome the VEP approach can make at least three contributions: first, it provides a non-invasive approach towards the evaluation of the best placement of the SEEG electrodes. This is accomplished via the evaluation of the hypothesis on EZ as based on presurgical evaluation. Because VEP models are generative models capable of realistically producing clinically used non-invasive imaging signals (EEG, MEG, fMRI), different EZ hypotheses can be confronted directly against imaging data. Second, following invasive SEEG exploration, the EZ hypotheses can be improved, fit to the data and further tested via stimulation paradigms as we demonstrated here. Systematic stimulation of target zones in the VEP network aids in further sharpening of the delineation of the EZ and in achieving a better understanding of the overall functional organization of the network. Third, surgical strategies can be systematically tested within the VEP model. So far traditional approaches to surgery apply one focal resection or ablation at the hypothesized EZ, based on the dogmatic concept that medically refractory epilepsy is ultimately a focal disease. A large unknown remains the size, the number and the specific anatomical location of possible resections or thermal lesions designed to modulate large-scale epileptic networks. VEP models allow not only to parametrically vary the size of the resection focus, but also to employ multiple lesions at different locations making thus full use of the network nature of the VEP model. Technically this is possible nowadays: stereotactic-guided laser technology, for instance, permits the modulation of large-scale networks by allowing the placement of multiple lesions in key components of previously mapped epileptic networks.

Key to the success of this approach will be the VEP model fitting against empirical data. This approach identifies the individual VEP in its own personalized parameter space. Fitting high-dimensional nonlinear models to data remains, however, a general challenge for machine learning techniques. The same nonlinear VEP model may generate dynamics leading to an infinite number of different realizations, i.e. evolutions in time, possibly multistability with strong dependence on initial conditions and stochastic contributions (noise), as well as external perturbations in the case of stimulation. In principle, model inversion of such a generative model requires extensive sampling of the state space and long observation times, both of which are requirements that cannot be easily satisfied in most clinical applications. Data fitting is also rendered more tractable by ignoring time delays in interareal communication. This is justified by our focus on seizure propagation and its coupling via the slow permittivity variable. By this approach, we lose however the ability to predict the spatial synchronization patterns on the time scale of fast oscillations. The VEP brain model under this approximation is comparable to firing rate-based models, which have been successfully used in connectome based brain network modeling of the resting state (Deco et al., 2011). These models typically also neglect the signal transmission delays with the justification that the oscillations are not considered explicitly, but only through fixed-point models of firing rate.

In VEP models we can take advantage of pathology and patient specific constraints on model structure and priors that enable clinically useful estimations. Here we used the patient's structural connectivity and MRI lesion, adapting it based on clinical, anatomical and functional information specific to this patient, and applied an inversion of the model to one of the patient's complex seizures. We obtained plausible time courses for network activity and spatial distribution of the epileptogenicity parameter. Additional constraints to the model dynamics may also be derived from statistical descriptions of the neuroimaging data in the form of neuromarkers. In the case of epilepsy, examples of such neuromarkers would include the recruitment probabilities and associated time delays, functional connectivity, and epileptogenicity indices (Bartolomei et al., 2008) among others.

To our knowledge no other computational approaches towards the delineation of the EZ exist with one notable exception. (Burns et al., 2014) used graph theoretical metrics, in particular centrality, applied to intracranial EEG (iEEG) signals. The one common phenomenon across patients, regardless of what motif they exhibit in some of their iEEG recordings, is that immediately prior to seizures, one or a few channels typically differentiate from the others. These few channels become “disconnected” or the least “central” to the network near seizure onset because of their sudden atypical activity. Near seizure termination, the pathological activity settles and these channels return to their average activity and hence average inter-ictal centrality. (Burns et al., 2014) compute the network centrality for each channel as a function of time before, during and after seizure, and use the centrality time course to delineate the EZ. The success of this approach further underwrites the network nature of epilepsy.

Acknowledgements

The research reported herein was supported by the Brain Network Recovery Group (220020255) through the James S. McDonnell Foundation and funding from the European Union Seventh Framework Programme Human Brain Project (grant no. 60402), Agence National de la Recherche “Vibrations” (ANR 13 PRTS 0011 01) and within the FHU EPINEXT by the A*MIDEX project (ANR-11-IDEX-0001-02) funded by the "Investissements d'Avenir" French Governement program managed by the French National Research Agency (ANR).

References

Adelson, P.D., O'Rourke, D.K., Albright, A.L., 1995. Chronic invasive monitoring for identifying seizure foci in children. Neurosurg. Clin. N. Am. 6, 491–504.

Ahmadi, M.E., Hagler, D.J., McDonald, C.R., Tecoma, E.S., Iragui, V.J., Dale, A.M., Halgren, E., 2009. Side matters: diffusion tensor imaging tractography in left and right temporal lobe epilepsy. AJNR. Am. J. Neuroradiol. 30, 1740–1747.

Allen, E.A., Damaraju, E., Plis, S.M., Erhardt, E.B., Eichele, T., Calhoun, V.D., 2012. Tracking whole-brain connectivity dynamics in the resting state. Cereb. Cortex 1–14. http://dx.doi.org/10.1093/cercor/bhs352.

Bartolomei, F., Chauvel, P., Wendling, F., 2008. Epileptogenicity of brain structures in human temporal lobe epilepsy: a quantified study from intracerebral EEG. Brain 131, 1818–1830. http://dx.doi.org/10.1093/brain/awn111.

Bartolomei, F., Guye, M., Wendling, F., 2013. Abnormal binding and disruption in large scale networks involved in human partial seizures. EPJ Nonlinear Biomed. Phys. 1, 4.

Bernhardt, B.C., Hong, S., Bernasconi, A., Bernasconi, N., 2013. Imaging structural and functional brain networks in temporal lobe epilepsy. Front. Hum. Neurosci. 7, 1–14. http://dx.doi.org/10.3389/fnhum.2013.00624.

Besson, P., Dinkelacker, V., Valabregue, R., Thivard, L., Leclerc, X., Baulac, M., Sammler, D., Colliot, O., Lehéricy, S., Samson, S., Dupont, S., 2014. Structural connectivity differences

in left and right temporal lobe epilepsy. NeuroImage 100, 135–144. http://dx.doi.org/10.1016/j.neuroimage.2014.04.071.
Bonilha, L., Nesland, T., Martz, G.U., Joseph, J.E., Spampinato, M.V., Edwards, J.C., Tabesh, A., 2012. Medial temporal lobe epilepsy is associated with neuronal fibre loss and paradoxical increase in structural connectivity of limbic structures. J. Neurol. Neurosurg. Psychiatry 83, 903–909.
Bricolo, A., Turazzi, S., Faccioli, F., Odorizzi, F., Sciaretta, G., Erculiani, P., 1978. Clinical application of compressed spectral array in long-term EEG monitoring of comatose patients. Electroencephalogr. Clin. Neurophysiol. 45, 211–225.
Bulacio, J.C., Jehi, L., Wong, C., Gonzalez-Martinez, J., Kotagal, P., Nair, D., Najm, I., Bingaman, W., 2012. Long-term seizure outcome after resective surgery in patients evaluated with intracranial electrodes. Epilepsia 53, 1722–1730. http://dx.doi.org/10.1111/j.1528-1167.2012.03633.x.
Burns, S.P., Santaniello, S., Yaffe, R.B., Jouny, C.C., Crone, N.E., Bergeyc, G.K., Anderson, W.S., Sarma, S.V., 2014. Network dynamics of the brain and influence of the epileptic seizure onset zone. Proc. Natl. Acad. Sci. U. S. A. 111, E5321–E5330. http://dx.doi.org/10.1073/pnas.1401752111.
Deco, G., Kringelbach, M.L., 2014. Great expectations: using whole-brain computational connectomics for understanding neuropsychiatric disorders. Neuron. 84 (5), 892–905. http://dx.doi.org/10.1016/j.neuron.2014.08.034.
Deco, G., Jirsa, V., McIntosh, A.R., Sporns, O., Kötter, R., 2009. Key role of coupling, delay, and noise in resting brain fluctuations. Proc. Natl. Acad. Sci. U. S. A. 106, 10302–10307. http://dx.doi.org/10.1073/pnas.0901831106.
Deco, G., Jirsa, V.K., McIntosh, A.R., 2011. Emerging concepts for the dynamical organization of resting-state activity in the brain. Nat. Rev. Neurosci. 12, 43–56. http://dx.doi.org/10.1038/nrn2961.
Deco, G., McIntosh, A.R., Shen, K., Hutchison, R.M., Menon, R.S., Everling, S., Hagmann, P., Jirsa, V.K., 2014. Identification of optimal structural connectivity using functional connectivity and neural modeling. J. Neurosci. 34, 7910–7916. http://dx.doi.org/10.1523/JNEUROSCI.4423-13.2014.
DeSalvo, M.N., Douw, L., Tanaka, N., Reinsberger, C., Stufflebeam, S.M., 2014. Altered structural connectome in temporal lobe epilepsy. Radiology 270, 842–848.
El Houssaini, K., Ivanov, A.L., Bernard, C., Jirsa, V.K., 2015. Seizures, refractory status epilepticus, and depolorization block as endogenous brain activities. Phys. Rev. E. 91, 010701.
Falcon, I., Riley, J.D., Jirsa, V.K., McIntosh, A.R., Shereen, A.D., Chen, E.E., Solodkin, A., 2015. The Virtual Brain: Modeling Biological Correlates of Recovery after chronic stroke. Frontiers (Boulder).
Finn, E.S., Shen, X., Scheinost, D., Rosenberg, M.D., Huang, J., Chun, M.M., Papademetris, X., Constable, R.T., 2015. Functional connectome fingerprinting: identifying individuals using patterns of brain connectivity. Nat. Neurosci. (advance on).
Fischl, B., 2012. FreeSurfer. NeuroImage 62, 774–781. http://dx.doi.org/10.1016/j.neuroimage.2012.01.021.
Friston, K.J., Stephan, K.E., Montague, R., Dolan, R.J., 2014. Computational psychiatry: the brain as a phantastic organ. Lancet Psychiatry 1, 148–158. http://dx.doi.org/10.1016/S2215-0366(14)70275-5.
Fuhrmann, S., Ackermann, J., Kalbe, T., Goesele, M., 2010. Direct Resampling for Isotropic Surface Remeshing. Vision, Modeling, and Visualization, pp. 1–28. http://dx.doi.org/10.2312/PE/VMV/VMV10/009–016.
Ghosh, A., Rho, Y., McIntosh, A.R., Kötter, R., Jirsa, V.K., 2008. Noise during rest enables the exploration of the brain's dynamic repertoire. PLoS Comput. Biol. 4, e1000196. http://dx.doi.org/10.1371/journal.pcbi.1000196.
Gramfort, A., Papadopoulo, T., Olivi, E., Clerc, M., 2010. OpenMEEG: opensource software for quasistatic bioelectromagnetics. Biomed. Eng. Online 9, 45. http://dx.doi.org/10.1186/1475-925X-9-45.
Hansen, E.C.A., Battaglia, D., Spiegler, A., Deco, G., Jirsa, V.K., 2014. Functional Connectivity Dynamics: modeling the switching behavior of the resting state. NeuroImage 105, 525–535. http://dx.doi.org/10.1016/j.neuroimage.2014.11.001.
Heinemann, U., Konnerth, A., Pumain, R., Wadman, W.J., 1986. Extracellular calcium and potassium concentration changes in chronic epileptic brain tissue. Adv. Neurol. 44, 641–661.
Hoffman, M.D., Gelman, A., 2011. The No-U-Turn Sampler: Adaptively Setting Path Lengths in Hamiltonian Monte Carlo. arXiv Prepr, pp. 1–30.
Honey, C.J., Kötter, R., Breakspear, M., Sporns, O., 2007. Network structure of cerebral cortex shapes functional connectivity on multiple time scales. Proc. Natl. Acad. Sci. U. S. A. 104, 10240–10245. http://dx.doi.org/10.1073/pnas.0701519104.
Ikeda, A., Taki, W., Kunieda, T., Terada, K., Mikuni, N., Nagamine, T., Yazawa, S., Ohara, S., Hori, T., Kaji, R., Kimura, J., Shibasaki, H., 1999. Focal ictal direct current shifts in human epilepsy as studied by subdural and scalp recording. Brain 122, 827–838. http://dx.doi.org/10.1093/brain/122.5.827.
Jayakar, P., 1999. Invasive EEG monitoring in children: when, where, and what? J. Clin. Neurophysiol. 116, 408.
Jayakar, P., Duchowny, M., Resnick, T.J., 1994. Subdural monitoring in the evaluation of children for epilepsy surgery. J. Child Neurol. 9. http://dx.doi.org/10.1177/08830738940090020 91 (2S61–2S66).
Jeha, L.E., Najm, I., Bingaman, W., Dinner, D., Widdess-Walsh, P., Luders, H., 2007. Surgical outcome and prognostic factors of frontal lobe epilepsy surgery. Brain 130, 574–584. http://dx.doi.org/10.1093/brain/awl364.
Jenkinson, M., Beckmann, C.F., Behrens, T.E.J., Woolrich, M.W., Smith, S.M., 2012. FSL. NeuroImage 62, 782–790.
Jirsa, V.K., 2009. Neural field dynamics with local and global connectivity and time delay. Philos. Transact. A Math. Phys. Eng. Sci. 367, 1131–1143. http://dx.doi.org/10.1098/rsta.2008.0260.
Jirsa, V.K., Jantzen, K.J., Fuchs, A., Kelso, J.A.S., 2002. Spatiotemporal forward solution of the EEG and MEG using network modeling. IEEE Trans. Med. Imaging 21, 493–504. http://dx.doi.org/10.1109/TMI.2002.1009385.
Jirsa, V.K., Sporns, O., Breakspear, M., Deco, G., McIntosh, A.R., 2010. Towards the virtual brain: network modeling of the intact and the damaged brain. Arch. Ital. Biol. 148, 189–205.
Jirsa, V.K., Stacey, W.C., Quilichini, P.P., Ivanov, A.I., Bernard, C., 2014. On the nature of seizure dynamics. Brain 137, 2210–2230. http://dx.doi.org/10.1093/brain/awu133.
Johansen-Berg, H., Berhens, T.E.J., 2009. Diffusion MRI: From Quantitative Measurement to in vivo Neuroanatomy. Elsevier.
Knösche, T.R., Anwander, A., Liptrot, M., Dyrby, T.B., 2015. Validation of tractography: Comparison with manganese tracing. Hum. Brain Mapp. 36, 4116–4134. http://dx.doi.org/10.1002/hbm.22902.
Kucukelbir, A., Ranganath, R., Gelman, A., Blei, D.M., 2015. Automatic Variational Inference in Stan. arXiv Prepr, pp. 1–22.
Lopez-Gonzalez, M.A., Gonzalez-Martinez, J.A., Jehi, L., Kotagal, P., Warbel, A., Bingaman, W., 2012. Epilepsy surgery of the temporal lobe in pediatric population: a retrospective analysis. Neurosurgery 70, 684–692. http://dx.doi.org/10.1227/NEU.0b013e318235183d.
Makeig, S., 1993. Auditory event-related dynamics of the EEG spectrum and effects of exposure to tones. Electroencephalogr. Clin. Neurophysiol. 86, 283–293.
Markram, H., Muller, E., Ramaswamy, S., Reimann, M.W., Abdellah, M., Sanchez, C.A., Ailamaki, A., Alonso-Nanclares, L., Antille, N., Arsever, S., Kahou, G.A.A., Berger, T.K., Bilgili, A., Buncic, N., Chalimourda, A., Chindemi, G., Courcol, J.-D., Delalondre, F., Delattre, V., Druckmann, S., Dumusc, R., Dynes, J., Eilemann, S., Gal, E., Gevaert, M.E., Ghobril, J.-P., Gidon, A., Graham, J.W., Gupta, A., Haenel, V., Hay, E., Heinis, T., Hernando, J.B., Hines, M., Kanari, L., Keller, D., Kenyon, J., Khazen, G., Kim, Y., King, J.G., Kisvarday, Z., Kumbhar, P., Lasserre, S., Le Bé, J.-V., Magalhães, B.R.C., Merchán-Pérez, A., Meystre, J., Morrice, B.R., Muller, J., Muñoz-Céspedes, A., Muralidhar, S., Muthurasa, K., Nachbaur, D., Newton, T.H., Nolte, M., Ovcharenko, A., Palacios, J., Pastor, L., Perin, R., Ranjan, R., Riachi, I., Rodríguez, J.-R., Riquelme, J.L., Rössert, C., Sfyrakis, K., Shi, Y., Shillcock, J.C., Silberberg, G., Silva, R., Tauheed, F., Telefont, M., Toledo-Rodriguez, M., Tränkler, T., Van Geit, W., Díaz, J.V., Walker, R., Wang, Y., Zaninetta, S.M., DeFelipe, J., Hill, S.L., Segev, I., Schürmann, F., 2015. Reconstruction and simulation of neocortical microcircuitry. Cell 163, 456–492. http://dx.doi.org/10.1016/j.cell.2015.09.029.
Najm, I.M., Naugle, R., Busch, R.M., Bingaman, W.E., Lüders, H.O., 2006. Definition of the epileptogenic zone in a patient with non-lesional temporal lobe epilepsy arising from the dominant hemisphere. Epileptic Disord. 8, 27–35.
Nakagawa, T.T., Jirsa, V.K., Spiegler, A., McIntosh, A.R., Deco, G., 2013. Bottom up modeling of the connectome: linking structure and function in the resting brain and their changes in aging. NeuroImage 80, 318–329. http://dx.doi.org/10.1016/j.neuroimage.2013.04.055.
Proix, T., Bartolomei, F., Chauvel, P., Bernard, C., Jirsa, V.K., 2014. Permittivity coupling across brain regions determines seizure recruitment in partial epilepsy. J. Neurosci. 34, 15009–15021. http://dx.doi.org/10.1523/JNEUROSCI.1570-14.2014.
Proix, T., Bartolomei, F., Guye, M., Jirsa, V.K., 2016a. Individual structural connectivity outlines recruitment networks in partial epilepsy (under review) .
Proix, T., Spiegler, S., Schirner, M., Rothmeier, S., Ritter, P., Viktor, K., 2016b. Using structural and diffusion MRI in large-scale brain models: preprocessing, sampling effects, and dynamics. NeuroImage. http://dx.doi.org/10.1016/j.neuroimage.2016.06.016.
Rosenow, F., Lüders, H., 2001. Presurgical evaluation of epilepsy. Brain 124, 1683–1700.
Sanz Leon, P., Knock, S.A., Woodman, M.M., Domide, L., Mersmann, J., McIntosh, A.R., Jirsa, V., 2013. The Virtual Brain: a simulator of primate brain network dynamics. Front. Neuroinform. 7, 10. http://dx.doi.org/10.3389/fninf.2013.00010.
Sanz-Leon, P., Knock, S.A., Spiegler, A., Jirsa, V.K., 2015. Mathematical framework for large-scale brain network modelling in The Virtual Brain. NeuroImage 1 (111), 385–430. http://dx.doi.org/10.1016/j.neuroimage.2015.01.002.
Sarvas, J., 1987. Basic mathematical and electromagnetic concepts of the biomagnetic inverse problem. Phys. Med. Biol. 32, 11.
Schirner, M., Rothmeier, S., Jirsa, V.K., McIntosh, A.R., Ritter, P., 2015. An automated pipeline for constructing personalized virtual brains from multimodal neuroimaging data. NeuroImage 117, 343–357. http://dx.doi.org/10.1016/j.neuroimage.2015.03.055.
Seehaus, A.K., Roebroeck, A., Chiry, O., Kim, D.-S., Ronen, I., Bratzke, H., Goebel, R., Galuske, R.A.W., 2013. Histological validation of DW-MRI tractography in human postmortem tissue. Cereb. Cortex 23, 442–450. http://dx.doi.org/10.1093/cercor/bhs036.
Smith, R.E., Tournier, J.-D., Calamante, F., Connelly, A., 2012. Anatomically-constrained tractography: improved diffusion MRI streamlines tractography through effective use of anatomical information. NeuroImage 62, 1924–1938.
Smith, R.E., Tournier, J.-D., Calamante, F., Connelly, A., 2013. SIFT: Spherical-deconvolution informed filtering of tractograms. NeuroImage 67, 298–312.
Spiegler, A., Jirsa, V., 2013. Systematic approximations of neural fields through networks of neural masses in the virtual brain. NeuroImage 83, 704–725.
Spiegler, A., Hansen, E.C.A., McIntosh, A.R., Jirsa, V.K., 2016. Modeling the critical brain: stimulation, dissipation and resting state networks. eNeuro (in press).
Sporns, O., Tononi, G., Kötter, R., 2005. The Human Connectome: A Structural Description of the Human Brain. PLoS Comput. Biol. 1 (4), e42. http://dx.doi.org/10.1371/journal.pcbi.0010042.
Stephan, K.E., Mathys, C., 2014. Computational approaches to psychiatry. Curr. Opin. Neurobiol. 25, 85–92. http://dx.doi.org/10.1016/j.conb.2013.12.007.
Stephan, K.E., Iglesias, S., Heinzle, J., Diaconescu, A.O., 2015. Translational perspectives for computational neuroimaging. Neuron 87, 716–732. http://dx.doi.org/10.1016/j.neuron.2015.07.008.
Suh, M., Ma, H., Zhao, M., Sharif, S., Schwartz, T.H., 2006. Neurovascular coupling and oximetry during epileptic events. Mol. Neurobiol. 33, 181–197. http://dx.doi.org/10.1385/MN:33:3:181.
Talairach, J., Bancaud, J., 1966. Lesion, "Irritative" Zone and Epileptogenic focus. Stereotact. Funct. Neurosurg. 27, 91–94.
The Stan Development Team, 2015. Stan: A C++ Library for Probability and Sampling.

Tournier, J.-D., Calamante, F., Connelly, A., 2007. Robust determination of the fibre orientation distribution in diffusion MRI: non-negativity constrained super-resolved spherical deconvolution. NeuroImage 35, 1459–1472. http://dx.doi.org/10.1016/j.neuroimage.2007.02.016.

Vanhatalo, S., Holmes, M.D., Tallgren, P., Voipio, J., Kaila, K., Miller, J.W., 2003. Very slow EEG responses lateralize temporal lobe seizures: an evaluation of non-invasive DC-EEG. Neurology 60, 1098–1104. http://dx.doi.org/10.1212/01.WNL.0000052993.37621.CC.

Widdess-Walsh, P., Jeha, L., Nair, D., Kotagal, P., Bingaman, W., Najm, I., 2007. Subdural electrode analysis in focal cortical dysplasia: Predictors of surgical outcome. Neurology 69, 660–667. http://dx.doi.org/10.1212/01.wnl.0000267427.91987.21.

Wirsich, J., Perry, A., Ridley, B., Proix, T., Golos, M., Bénar, C.J., Ranjeva, J.P., Bartolomei, F., Breakspear, M., Jirsa, Viktor, K., Guye, M., 2016. Whole-brain analytic measures of network communication reveal increased structure-function correlation in temporal lobe epilepsy. Neuroimage Clin. 19 (11), 707–718.

Wyllie, E., Lüders, H., Morris, H.H., Lesser, R.P., Dinner, D.S., Rothner, A.D., Erenberg, G., Cruse, R., Friedman, D., Hahn, J., 1988. Subdural electrodes in the evaluation for epilepsy surgery in children and adults. Neuropediatrics 19, 80–86.

Zhao, M., Nguyen, J., Ma, H., Nishimura, N., Schaffer, C.B., Schwartz, T.H., 2011. Preictal and ictal neurovascular and metabolic coupling surrounding a seizure focus. J. Neurosci. 31, 13292–13300.